

Contents lists available at ScienceDirect

Marine Structures

journal homepage: http://www.elsevier.com/locate/marstruc





Active heave compensation of floating wind turbine installation using a catamaran construction vessel

Zhengru Ren a,b,* , Roger Skjetne a,b , Amrit Shankar Verma a,b,c , Zhiyu Jiang d , Zhen Gao a,b , Karl Henning Halse a,e

- a Centre for Research-based Innovation on Marine Operations (SFI MOVE), Norwegian University of Science and Technology (NTNU), Norway
- ^b Department of Marine Technology, NTNU, NO-7491, Trondheim, Norway
- c Faculty of Aerospace Engineering, Aerospace Manufacturing Technologies, Delft University of Technology (TU Delft), Delft, 2629 HS, Netherlands
- ^d Department of Engineering Sciences, University of Agder, 4879, Grimstad, Norway
- ^e Department of Ocean Operations and Civil Engineering, NTNU, Norway

ARTICLE INFO

Keywords: Floating offshore wind turbine Marine operations Wind turbine installation Heave compensator Hydraulic system Singular perturbation theory

ABSTRACT

The application of floating wind turbines is limited by the high cost that increases with the water depth. Offshore installation and maintenance continue to consume a high percentage of the project budget. To improve the installation efficiency of the floating offshore wind turbine, a novel concept is proposed by the SFI MOVE project. Several wind turbine superstructure components are preassembled onshore and carried to the installation site by a catamaran construction vessel. Each assembly can then be installed using only one lift, and the concept is less sensitive to weather conditions. In this paper, a control algorithm of the proposed hydraulic active heave compensator system is developed using singular perturbation theory to cancel the relative motion between the spar top and gripped preassembly bottom. Closed-loop stability is proven, and the simulation results show that the installation efficiency is improved with an increase in the acceptable weather conditions.

1. Introduction

The wind energy market has grown steadily in recent decades, and the trend is expected to continue in the future. The price and stability of wind power are gradually improving. Offshore wind power technology is increasingly matured because of the advanced design and intelligent control algorithms. Compared to onshore wind energy, offshore wind power is more competitive in the energy market due to its better electric power quality. However, the price of offshore wind energy is still several times higher than that of the onshore wind energy, though the gap is filled by continuous research, more qualified technology, and better state-of-the-art solutions. The costly support foundations and high expense of offshore installation and maintenance account for the high price of offshore wind turbines (OWTs) [1]. The installation and maintenance costs will rise considering the foreseen growth of the floating OWTs in the deep-water applications [2–5].

There are several OWT installation strategies according to the level of onshore preassembly [6]. For example, the single blade installation approach requires the shortest offshore transportation time and is suitable for large-scale OWTs. To enhance the

^{*} Corresponding author. Department of Marine Technology, NTNU, NO-7491, Trondheim, Norway. E-mail addresses: zhengru.ren@ntnu.no (Z. Ren), roger.skjetne@ntnu.no (R. Skjetne), a.s.verma@tudelft.nl (A.S. Verma), zhiyu.jiang@uia.no (Z. Jiang), zhen.gao@ntnu.no (Z. Gao), karl.h.halse@ntnu.no (K.H. Halse).

installation efficiency, a number of studies on single blade installation have been conducted, e.g., minimization of installation cost and time [7,8], installation criteria [9,10], impact analysis [11], optimal scheduling [12], lifting operation [13], mating operation [14], and real-time hub motion estimation [15]. The motion and position monitoring system developed by Tian et al. [16] for offshore structure installation has been demonstrated with centimeter-level accurcy in field operation, which can be used to effectively improve the installation efficiency of OWTs. A higher level of onshore integration demands shorter offshore installation time, such as the bunny-ear configuration. A novel OWT installation concept proposed by the SFI MOVE project allows a more efficient installation of floating OWT by using a catamaran installation vessel [17,18]. The system performance is improved by introducing automatic control; e.g., a roll-reduction system is studied in Ref. [19]. The mating scenario proposed is similar to the mating process between a suspended wind turbine blade and hub studied in Refs. [18,20]. The studies based on landing forces show that the guide pins would deform and even damage if the impact velocity between the blade root center and hub center exceeds a speed limitation. Allowable impact velocities are obtained through finite element analysis, for example, 0.76 m/s for sideways impact and 1.35 m/s for head-on impact [20]. Similarly, the critical relative velocities between the preassembly and spar foundation in a mating operation can be found through finite element analysis given contact stiffnesses of the spar top and the tower bottom 18.

Automatic control and onboard decision support algorithms have been applied in a variety of marine systems to enhance operational efficiency and safety, for example, onboard sea state estimation [21], trajectory planning [22], and model identification [23]. Heave compensation systems are widely used in the offshore operations, which are categorized into passive schemes and active schemes according to the existence of control inputs [24]. Allowing operations in higher sea states, an active hydraulic heave compensator (AHC) compensates the effects of wave-induced vessel heave motions using feedback control [25,26].

Industrial hydraulic systems are widely used mainly due to their attractive characteristics, i.e., high power to weight ratio, high stiffness, simple structure, economical benefits, etc. [27] The dynamic responses of the catamaran-spar system and installation criteria are studied in Ref. [18]. The preliminary results of a simple AHC are presented in Ref. [28] with an emphasis on the system dynamics. This paper extends [28] with an emphasis on the control design. A control algorithm of the proposed hydraulic AHC system is developed using singular perturbation theory. This allows a simpler control law to be derived, with necessary stability properties (global exponential stability), as opposed to using e.g. backstepping or feedback linearization - which would typically result in complex control algorithms with many feedback cancellation terms [29,30]. Besides, the trajectory planning module is improved to accomplish smooth lifting and lowering operations. Numerical verification is conducted on a high-fidelity model.

This paper is organized as follows. Section 2 briefly addresses the system and the modeling process. A simplified one-dimensional model is presented to design the controller. In Section 3, the trajectory planning system and feedback control system are developed. The pole placement technique and singular perturbation theory are adopted to design the controller and prove the system stability. In Section 4, the proposed control system is verified by numerical simulations. Section 5 summarizes the results of the paper.

1.1. Preliminary

Before going into details, a lemma is introduced.

Lemma 1. (Theorem 11.3 in [31]).

Consider the singularly perturbed system

$$\dot{x} = f(x, z), f(0, 0) = 0,$$
 (1a)

$$\varepsilon \dot{z} = g(x, z), \ g(0, 0) = 0,$$
 (1b)

where f and g are locally Lipschitz in a domain that contains the origin (x,z)=(0,0). Let $z=\rho(x)$ be the isolated root of g(x,z)=0 and suppose $\rho(0)=0$. Define $y:=z-\rho(z)$ and assume there are Lyapunov functions V(x) and V(x,y) that satisfy:

- 1. $\frac{\partial V}{\partial x}f(x,\rho(x)) \leq -\alpha_1\psi_1^2(x), \forall x \in \mathbb{D}_x$
- 2. $\frac{\partial W}{\partial x}g(x,y+\rho(x)) \leq -\alpha_2\psi_2^2(y), \forall (x,y) \in \mathbb{D}_x \times \mathbb{D}_y$
- 3. $W_1(y) \leq W(x,y) \leq W_2(y), \forall (x,y) \in \mathbb{D}_x \times \mathbb{D}_y$
- 4. $\frac{\partial V}{\partial x}[f(x,y+\rho(x))-f(x,\rho(x))] \leq \beta_1 \psi_1(x)\psi_2(y)$

$$5. \ \left[\frac{\partial \mathbf{W}}{\partial \mathbf{x}} - \frac{\partial \mathbf{W}}{\partial \mathbf{y}} \frac{\partial \rho}{\partial \mathbf{x}} \right] \! f(\mathbf{x}, \mathbf{y} + \rho(\mathbf{x})) \leq \beta_2 \psi_1(\mathbf{x}) \psi_2(\mathbf{y}) + \gamma \psi_2^2(\mathbf{y}),$$

where domain $\mathbb{D}_x \subset \mathbb{R}^n$ contains x=0, domain $\mathbb{D}_y \subset \mathbb{R}^m$ contains y=0, and the constants α_1 , α_2 , β_1 , β_2 , and γ are nonnegative. Functions $\psi_1(x)$ and $\psi_2(y)$ are positive definite, i.e., $\psi_1(0)=0$, $\psi_1(x)>0$, $\forall x\in \mathbb{D}_x/\{0\}$, and $\psi_2(0)=0$, $\psi_2(y)>0$, $\forall y\in \mathbb{D}_y/\{0\}$. The origin of (1) is asymptotically stable for all $0<\varepsilon<\varepsilon^*$, where $\varepsilon^*:=\frac{\alpha_1\alpha_2}{\alpha_1\gamma+\beta_1\beta_2}$.

If V(x) is quadratic in x, $W_1(y)$ and $W_2(y)$ are quadratic in y, and $\psi_1(x) = |x|$ and $\psi_2(y) = |y|$, then the origin is exponentially stable.

¹ https://www.ntnu.edu/move.

If conditions (1) through (5) hold $\forall (x,y) \in \mathbb{R}^n \times \mathbb{R}^m$, then the stability is global.

2. Problem formulation

2.1. System description

The tower, nacelle, hub, and rotor have been fabricated and assembled onshore. The floating foundation has been installed. Hereafter, a spar foundation moored by several mooring lines is taken as an example. The system is illustrated in Fig. 1. After carrying the preassembled superstructure to the installation site by a catamaran, the mating operation starts. The horizontal positions and yaw orientation of the installation vessel are stabilized by the dynamic positioning (DP) system using a PID controller. The target is to place the upper structure onto the spar.

The superstructure is first lifted from the deck and transported to the aft. A hydraulic variable-displacement-controlled cylinder is adopted to compensate for the relative motion between the tower bottom and spar top. The preassembled wind turbine structure is rigidly gripped by the hydraulic device fixed at the aft of the catamaran and moves with the vessel. The following procedure is to execute the mating operation until the relative motion between the spar top and tower bottom satisfy the predefined criteria. The standard deviations (STDs) of the relative motions, including both relative displacement and velocity, are selected to evaluate the relative motion. Their critical values can be calculated through finite element analysis. The relative velocity is essential to the mating operation. In case of damaging the structures, the relative velocity should be bounded in a small safe range. Then, the preassembled structure is lowered to the spar foundation. The tower bottom is bolted and then released. The advantages of the proposed installation strategy ensure a higher efficiency and a shorter offshore operation period.

Since the gripper device constrains the horizontal relative motion between the spar top and tower bottom, the vertical head-on motion is crucial to the operation. Furthermore, decreasing relative motion improves operational safety and success. Hence, the expectation is to make the relative motion between the tower bottom and spar top as small as possible.

2.2. System modeling

A free-body diagram of the proposed system is shown in Fig. 2. Three right-hand reference frames are adopted, i.e., the local northeast-down (NED) coordinate system $\{n\}$, which is assumed to be inertial, the vessel body-fixed reference frame $\{b\}$, and the spar body-fixed reference frame $\{s\}$. In the NED coordinate system, the x^n -, y^n -, and z^n -axes point to the north, to the east, and downward, respectively, with an origin placed at the free water surface. In the body-fixed reference frames $\{b\}$ and $\{s\}$, the origin points are located at the vessel's and spar's center of gravity (COG), respectively. Consistent with the general definition, the x^b - and y^b -axes are directed to the bow and starboard, respectively. For the spar foundation, the x^s - and y^s -axes are not of importance due to the axial symmetry around the longitudinal z^s -axis. The vessel orientations about the x^n -, y^n -, and z^n -axes are roll (φ) , pitch (θ) , and yaw (ψ) , respectively.

2.2.1. Catamaran installation vessel and spar foundation

Unlike the decoupled simulations in [28], the simulation-verification model (SVM) adopted in this paper is a fully coupled model developed in the MATLAB/Simulink environment. In detail, the spar foundation and installation vessel are simulated as 6-degree-of-freedom (DOF) rigid bodies with force transfer functions calculated by ShipX using strip theory. The hydrodynamic interaction between the spar and vessel is ignored in this study, since the influence on the hydrodynamic loads is quite limited and the focus of this paper is on control design. Both floating structures are exposed to complex environments, including waves, current, and wind. The spar is moored by three mooring lines, which are simulated with the finite element method (FEM) models [32,33]. Current influences the relative inflow velocity at the spar and mooring lines. The current velocities at specific heights are calculated by interpolating the defined current profile from the free sea surface to the seafloor. The vessel is only influenced by the surface current. A sliding gripper

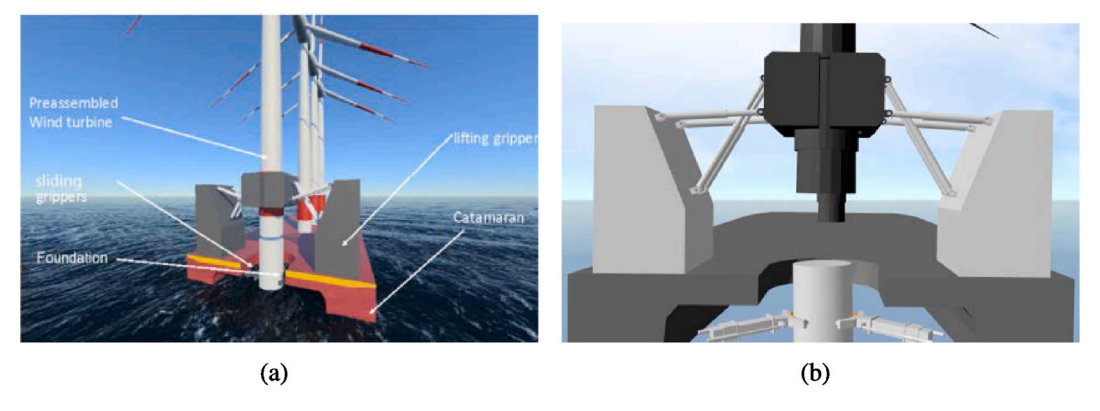


Fig. 1. Illustration of the proposed installation system: (a) overview; (b) close view.

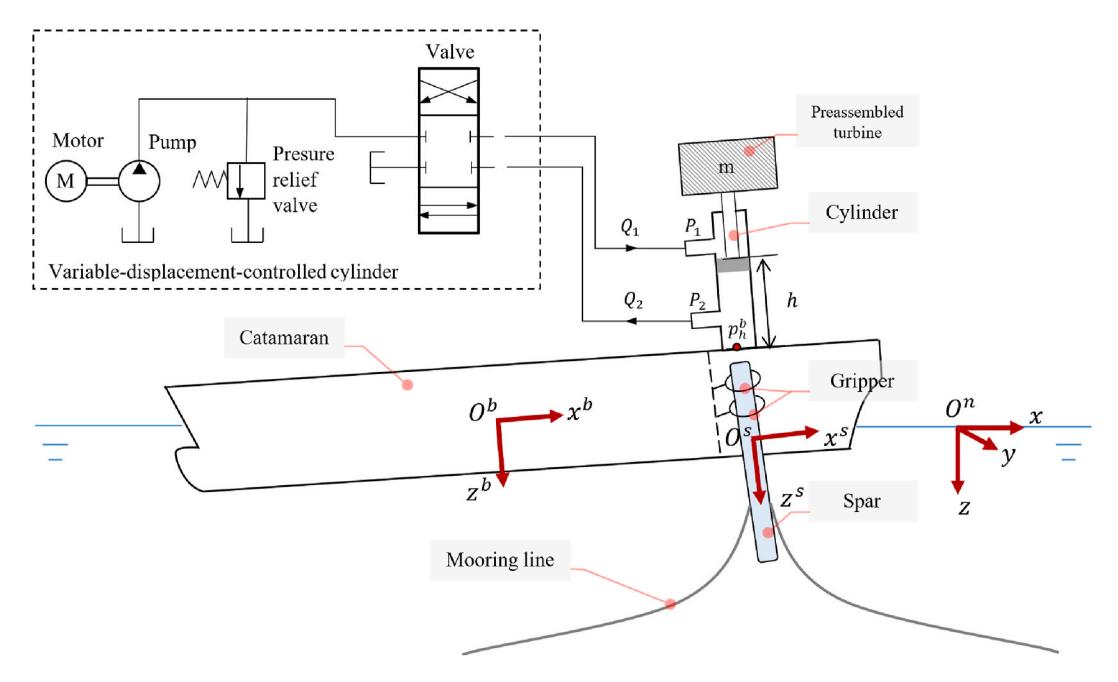


Fig. 2. Free-body diagram of the hydraulic active heave compensation system.

holds the spar foundation passively. The gripper is modeled as a pair of frictionless rings, i.e., planar springs fixed on the vessel in $\{b\}$. The springs provide restoring forces at the interconnection points between the spar and the rings on the x^b - and y^b -axes. The block diagram is shown in Fig. 3. Since the spar can still rotate when only one planar spring is employed, at least two planar springs are necessary to restrain the spar from rotating.

We assume that the preassembled structure is rigidly fixed on the vessel in $\{b\}$. The position of the tower bottom in $\{n\}$, $p_b \in \mathbb{R}^3$, is given by

$$p_b = p_v + R(\Phi)(p_b^b + d_h),$$
 (2)

where $p_v \in \mathbb{R}^3$ stands for the position of the catamaran COG in the local coordinate frame $\{n\}$, $R(\Phi) \in \mathbb{R}^{3\times 3}$ denotes the rotation matrix from the body-fixed to the NED reference frame with respect to the Euler angle vector $\Phi = [\varphi, \theta, \psi]^\top$, $p_h^b \in \mathbb{R}^3$ is the position of the hydraulic lifting device in $\{b\}$, and $d_h = [0, 0, -h]^\top \in \mathbb{R}^3$, where h > 0 refers to the moving distance of the lifting mechanism.

The velocity of the tower bottom in $\{n\}$, $v_b \in \mathbb{R}^3$, is given by the time derivative of (2), i.e.,

$$v_b = v_v + R(\Phi)S(\omega_v)(p_h^b + d_h) + R(\Phi)v_h, \tag{3}$$

where $v_v \in \mathbb{R}^3$ is the velocity of the catamaran COG in $\{n\}$, $S(\omega_v) \in \mathbb{R}^{3\times 3}$ is a skew-symmetric matrix used to present the cross product,

$$(M_{RB,v} + M_{A,v})\dot{\nu} + (C_{RB,v} + C_{A,v}(\nu))\nu + (D_v + D_{n,v}(\nu))v + g_v(\eta)$$

$$= \tau_{wave1,v} + \tau_{wave2,v} + \tau_{wind,v} + \tau_{thruster,v} + \sum_{i=1} \tau_{gv,i} + \tau_h,$$
(4)

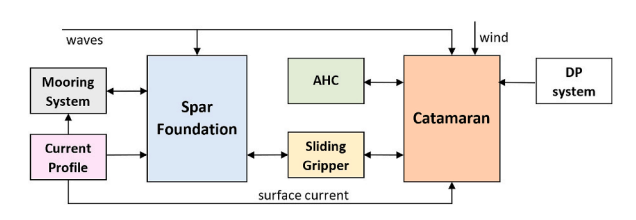


Fig. 3. Block diagram of the system.

 $\omega_v \in \mathbb{R}^3$ is the angular velocity vector, and $v_h = [0, 0, -\dot{h}]^\top \in \mathbb{R}^3$.

The models of the catamaran vessel and spar foundation are similar, given by

$$(M_{RB,s} + M_{A,s})\dot{\nu}_s + (C_{RB,s} + C_{A,s}(\nu_s))\nu_s + (D_s + D_{n,s}(\nu_s))\nu_s + g_s(\eta_s)$$

$$= \tau_{wave1,s} + \tau_{wave2,s} + \tau_{wind,s} + \tau_{thruster,s} + \sum_{i=1} \tau_{gs,i},$$
(5)

where $\eta = \operatorname{col}(p_{\nu}, \Phi) \in \mathbb{R}^{6}$ and $\eta_{s} = \operatorname{col}(p_{s}, \Phi_{s}) \in \mathbb{R}^{6}$ are the position and orientations of the vessel and spar foundation, $\Phi_{s} \in \mathbb{R}^{3}$ is the Euler angle vector of the spar foundation, $\nu \in \mathbb{R}^{6}$ and $\nu_{s} \in \mathbb{R}^{6}$ are the translational and rotational velocity of the vessel and spar foundation, $M_{RB} \in \mathbb{R}^{6 \times 6}$ and $M_{A} \in \mathbb{R}^{6 \times 6}$ are system inertia matrices of the rigid body and added mass, $C_{RB} \in \mathbb{R}^{6 \times 6}$ and $C_{A}(\nu) \in \mathbb{R}^{6 \times 6}$ are the Coriolis and centripetal matrices of the rigid body and added mass, $D \in \mathbb{R}^{6 \times 6}$ and $D_{n} \in \mathbb{R}^{6 \times 6}$ are linear and nonlinear damping matrices, $D_{s} \in \mathbb{R}^{6}$ are the restoring force and moment due to the buoyancy and gravity, $D_{s} \in \mathbb{R}^{6}$ are the restoring force and torque acting on the vessel and spar, and $D_{s} \in \mathbb{R}^{6 \times 6}$ and $D_{s} \in \mathbb{R}^{6 \times 6}$ are the vectors of forces and moments arising from first-order wave loads, second-order wave loads, wind loads, thruster loads, and hydraulic system, respectively.

The spar is rigidly fixed by the gripper in the body-fixed horizontal x^b - y^b plane at the interconnection points. The diagram of the gripper is presented in Fig. 4. The position of the gripper on the vessel is rigidly fixed at the aft. Due to the wave-induced heave loads, the spar foundation moves up and down in the z^b -direction. The relative motion between the spar foundation and assembly only exists in the vessel body-fixed z^b -axis.

The restoring force from the i^{th} gripper ring acting on the vessel in $\{n\}$ $f_{gv,1} \in \mathbb{R}^3$, is given by

$$f_{gv,i} = k_g (p_{gs,i} - p_{gv,i}), i = 1, 2,$$
 (6)

where $k_g \in \mathbb{R}$ is the stiffness of the gripper, $p_{gv} \in \mathbb{R}^3$ denotes the position of the gripper center, and $p_{gs} \in \mathbb{R}^3$ is the position of the interconnecting point on the spar longitude axis at the same height of the gripper center. Hence, the restoring force and torque acting on the vessel and spar in $\{b\}$ and $\{s\}$ are, respectively, given by

$$\tau_{gv,i} = \begin{bmatrix} R^{\top}(\mathbf{\Phi})f_{gv,i} \\ S(p_{gv,i}^b)R^{\top}(\mathbf{\Phi})f_{gv,i} \end{bmatrix} \text{ and } \tau_{gs,i} = \begin{bmatrix} -R^{\top}(\mathbf{\Phi}_s)f_{gv,i} \\ S(p_{gs,i}^s)R^{\top}(\mathbf{\Phi}_s)f_{gs,i} \end{bmatrix},$$
 (7)

where $p_{gv}^b \in \mathbb{R}^3$ and $p_{gs}^s \in \mathbb{R}^3$ are the distance vector from the interconnection point to the vessel and spar COG in $\{b\}$ and $\{s\}$, respectively.

Due to the large mass of the preassembly structure, the reacting forces and torques to the catamaran are not negligible and are given by

$$\tau_h = \begin{bmatrix} f_{h_v}^b \\ S(p_h^b) f_{h_v}^b \end{bmatrix},\tag{8}$$

where $f_{hv}^b = [0, 0, F_h]^{\top} \in \mathbb{R}^3$ and F_h is the reacting force from the hydraulic system acting on the vessel.

2.2.2. Active heave compensator

The spar foundation can only move in the z^b -direction due to the sliding gripper. Therefore, the proposed control problem is reduced to a one-dimensional system. A simplified variable-displacement controlled cylinder model is proposed in Ref. [34]. The model is simplified by assuming a constant density and an effective bulk modulus of the hydraulic fluid, as well as the neglected

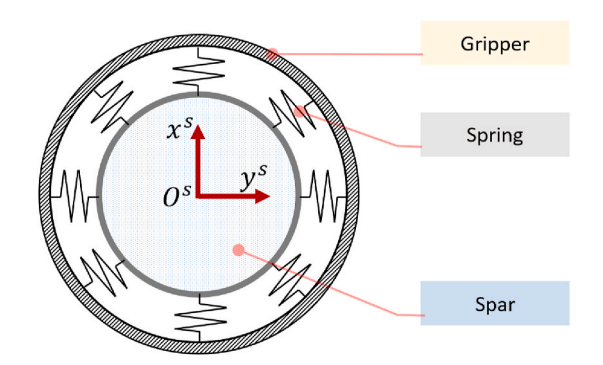


Fig. 4. Diagram of the sling gripper at the interconnection height.

influence from the pipelines. The rotation speed of the motor is assumed constant. The load pressure P is defined as

$$P = \begin{cases} P_1 - P_r, & \text{if } P_1 > P_r, \\ P_r - P_2, & \text{if } P_2 > P_r, \end{cases}$$
 (9)

where P_r denotes the constant return pressure, and P_1 and P_2 are the pressures on the two chambers of the cylinder.

The state-space model of the one-degree variable-displacement-controlled cylinder system on the z^b -axis is

$$\dot{h} = v$$
, (10a)

$$\dot{v} = \frac{1}{m}(-dv + PA + F_{ext}),\tag{10b}$$

$$\frac{V_h}{\beta}\dot{P} = -A\dot{h} - c_l P + u,\tag{10c}$$

where h is the moving distance of the lifting mechanism, v is the rate of change of the lifting mechanism, the input signal u is the product of the principal axis rotating speed of the pump and pump displacement, which is proportional to the input voltage, β is the bulk modulus of the hydraulic fluid, A is the area of the cylinder, c_l is the fluid leakage coefficient assumed constant, d is the coefficient of friction, and V_h is the effective volume of the cylinder, i.e., $V_h = V_{h0} + Ah$ where V_{h0} is the fluid volume in the pipelines, internal pump, etc. The total mass m is the combination of the mass of the hydraulic cylinder m_h and the mass of the lifted structure m_t , i.e., $m = m_h + m_t$. The external force F_{ext} is the component force of the gravity of the preassembly in the z^b -direction, which is approximated by $F_{ext} \cong mg\cos\theta\cos\phi$. Additionally, we know that $F_h = PA$.

2.3. Problem statement

The mating operation depends on the relative motion between the spar top and tower bottom, i.e., the relative velocity and relative displacement. The influences are twofold. First, the relative velocity determines the impact velocity and impact force between the structures. The mating flange and guiding pins could be damaged when the impact velocity is higher than the limits. Second, the success rate is decided by the relative displacement. The possibility of a successful plugin enhances with reduced relative displacement. Hence, an automated hydraulic heave compensator is introduced to reduce the relative motion.

A variable-displacement-controlled hydraulic cylinder is responsible for controlling the vertical motion of the preassembled wind turbine in $\{b\}$ by controlling the input u. We assume that the real-time position and orientations of the catamaran and the spar have been well measured.

There are two steps in the operation, i.e., lowering and mating. The preassembly should be lowered to the foundation slowly at time instant t_s to achieve the final mating operation. Additionally, the control objective of the mating operation is to control the relative motion between the tower bottom and the spar top mating point along the z^n -axis at a constant distance by commanding the hydraulic cylinder motion, that is, to make h(t) converge to $h_r(t)$ by applying approximate control effort on the input u, where $h_r(t)$ is the time-varying reference length of the cylinder.

3. Control system design

3.1. Trajectory planning module

In the process, the heave compensator should not only cancel the relative motion between the spar top and preassembly bottom but also slowly lower the preassembly to the spar foundation. Hence, the trajectory planning is categorized into two parts, i.e., the lengths of the cylinder to control the lower operation h_{d1} and to compensate the relative motion between the spar top and tower bottom h_{d2} . The lowering operation starts up at time instant t_s , i.e.,

$$h_{d1}(t) = \begin{cases} h_{d0}, & \text{if } t < t_s, \\ 0, & \text{if } t \ge t_s, \end{cases}$$
 (11)

where h_{d0} is the safety length of the pump before the lowering operation.

From Eq. (2), the desired length of the hydraulic piston for a successful mating operation is received from

$$h_{d2}(t_k) = [0, 0, 1] [p_h^b - R^\top (p_s(t_k) - p_v(t_k))].$$
 (12)

A reference model is used to generate smooth trajectories $h_{rj}(t)$ and $\dot{h}_{rj}(t)$ for a series of desired lengths h_{dj} , $j \in \{1,2\}$. The transfer function is given by

$$\frac{h_{rj}}{h_{dj}}(s) = \frac{\omega_{rj}^3}{\left(s + \omega_{rj}\right)\left(s^2 + 2\zeta_{rj}\omega_{ri} + \omega_{rj}^2\right)}, \ j \in \{1, 2\},\tag{13}$$

where ζ_r denotes the damping ratio and ω_r is the frequency. Select $\zeta_r = 1$ to ensure critical damping. The higher the ω_r is chosen, the faster the tracking dynamics will be. A reasonable ω_{r1} should be smaller than ω_{r2} . The overall reference signal becomes $h_r(t) = h_{r1}(t) + h_{r2}(t)$.

3.2. Control design

Since the bulk modulus of different kinds of fluid is always at a 10^9 N/m² level and V_h is normally less one $10\,m^3$, the high value of $\frac{\beta}{V_h}$ results in very fast pressure dynamics in (10c). The control algorithm requires very high and fast control efforts, which is practically impossible. Singular perturbation theory is useful to transfer a multiple-time-scale process into low-order models by dividing the system into a slow model and a fast model.

Since the vessel pitch and roll motions are limited, we assume that $F_{ext}=F_0+b$, where $F_0=mg$ is known and b is a constant unknown bias representing unmodeled dynamics. We assume b is constant; however, in practice, it will be slowly varying. Define three error states as $e_1:=h-h_r(t)$, $e_2:=\dot{e}_1=\nu-\dot{h}_r(t)$, and $e_0=\xi-\xi^*$, where $\xi:=\int_{t_0}^th(\tau)-h_r(\tau)d\tau$ is an integral action state and ξ^* is the unknown equilibrium for the integrator. Since P=0 is obviously not the equilibrium point, another state $\tilde{P}=P-P^*(t)$ is defined to denote the error between the real-time pressure P and the equilibrium pressure to compensate the payload's gravity $P^*(t)$. The error dynamic model is then transferred to the following form

$$\dot{e}_0 = e_1 \tag{14a}$$

$$\dot{e}_1 = e_2 \tag{14b}$$

$$\dot{e}_2 = -\frac{d}{m} \left(e_2 + \dot{h}_r \right) + \frac{A}{m} \left(\tilde{P} + P^* \right) + \frac{F_0 + b}{m} - \ddot{h}_r$$
 (14c)

$$\varepsilon \dot{\tilde{P}} = -A \left(e_2 + \dot{h}_r \right) - c_l \left(\tilde{P} + P^* \right) + u - \varepsilon \dot{P}^*,$$
 (14d)

where (14a)–(14c) is the slow model and (14d) is the fast model, and $\varepsilon = \frac{V_h}{g}$. Let

$$u = u_0 + \varepsilon \dot{P}^*. \tag{15}$$

where we will later show that $\dot{P}^*(t)$ is a known signal based on the reference signals.

Since this is a system with a two time scale behavior for ε small [35–37], let the fast time scale be $t_f = t/\varepsilon$ and define $x' := \frac{dx}{dt_f} = \frac{dx}{dt}$ $\frac{dt}{dt} = \varepsilon \dot{x}$. This gives the hydraulic system in the fast time scale,

$$e_0' = \varepsilon e_1$$
 (16a)

$$e_1^{\prime} = \varepsilon e_2$$
 (16b)

$$e_{2}' = \varepsilon \left[-\frac{d}{m} \left(e_{2} + \dot{h}_{r} \right) + \frac{A}{m} \left(\tilde{P} + P^{*} \right) + \frac{F_{0} + b}{m} - \ddot{h}_{r} \right]$$

$$(16c)$$

$$\tilde{P}' = -A\left(e_2 + \dot{h}_r\right) - c_l\left(\tilde{P} + P^*\right) + u_0. \tag{16d}$$

The fast response of \tilde{P} from (16d) is approximately described by the *boundary layer system* in Eq. (16d) for $\varepsilon=0$, where $(e_1',e_2',e_3')=0$. When in equilibrium, we require that $(e_1,e_2,e_3)=0$ and $\tilde{P}=0$. However, P^* is unknown yet. Setting $\tilde{P}'=0$ in (16d), the desired steady-state solution \tilde{P} to the boundary layer system becomes

$$\overline{\tilde{P}} = \frac{1}{c_I} \left[-A \left(e_2 + \dot{h}_r(\varepsilon t_f) \right) + u_0 \right] - P^*(\varepsilon t_f) = : \rho_1(e, u_0, \varepsilon t_f), \tag{17}$$

where $e = [e_0, e_1, e_2]^{\top} \in \mathbb{R}^3$. Equation (17) is substituted into (14a)–(14c) to get the *reduced system* $\dot{e}_0 = e_1$, $\dot{e}_1 = e_2$, and

$$\dot{e}_2 = \Upsilon u_0 + \Psi(e, t) + \frac{b}{m},\tag{18}$$

where $\Upsilon = \frac{A}{mc_l}$ is a positive constant (assuming that c_l is a known constant) and

$$\Psi(e,t) = -\left(\frac{d}{m} + A\Upsilon\right) \left(e_2 + \dot{h}_r(t)\right) + \frac{F_0}{m} - \ddot{h}_r(t). \tag{19}$$

In order to render the origin $(e_1, e_2, e_3) = 0$ uniformly globally exponentially stable (UGES) for the reduced system, the control u_0 is assigned as

$$u_0 = \frac{1}{r}(-\Psi(e,t) - c_0\xi - c_1e_1 - c_2e_2) =: \rho_2(e,t), \tag{20}$$

where c_0 , c_1 , and c_2 are positive constants.

For $u_0 = \rho_2(e, t)$ we inject (20) back into (17) and get the updated boundary layer solution $\rho(e, t) := \rho_1(e, \rho_2(e, t), t)$ according to

$$\rho(e,t) = \frac{1}{c_l} \left[-A \left(e_2 + \dot{h}_r(t) \right) - \frac{1}{r} (c_0 e_0 + c_1 e_1 + c_2 e_2) + \frac{1}{r} (-\Psi - c_0 \xi^*) \right] - P^*(t). \tag{21}$$

Since (21) is the solution to $\tilde{P}'=0$, calculating $\overline{\tilde{P}}=\rho(e,t)=0$ with e=0 results in the equilibrium pressure

$$P^*(t) = \frac{1}{A} \left[d\dot{h}_r(t) - F_0 + m\ddot{h}_r(t) - mc_0 \xi^* \right], \tag{22}$$

and from this the needed $\dot{P}^*(t)$ becomes

$$\dot{P}^*(t) = \frac{1}{A} \left[d\ddot{h}_r(t) + m\dot{h}_r(t) \right]. \tag{23}$$

Substituting (22) into (21) yields

$$\overline{\rho}(e) := -\frac{1}{A}Ce = \rho(e,t), \tag{24}$$

where $C = [mc_0, mc_1, mc_2 - d]$.

Defining $y := \tilde{P} - \overline{\rho}(e)$ and inserting (22) and (24) into (14a)–(14c), the resulting error dynamics becomes

$$\dot{e}_0 = e_1, \tag{25a}$$

$$\dot{e}_1 = e_2, \tag{25b}$$

$$\dot{e}_2 = \frac{A}{m} y - c_0 e_0 - c_1 e_1 - c_2 e_2,\tag{25c}$$

where we recognized ξ^* as $\frac{b}{c_0m}$. In vector form, after substituting (15), (20), and (22) into (14), the closed-loop hydraulic system (25) and (14d) is put into the standard form of singularly perturbed systems [31],

$$\dot{e} = A_0 e + B_0 y = A_0 e + B_0 \left(\tilde{P} - \overline{\rho}(e) \right) = : f\left(e, \tilde{P}\right), \tag{26a}$$

$$\varepsilon \dot{\tilde{P}} = -c_l y = -c_l \left(\tilde{P} - \overline{\rho}(e) \right) = : g\left(e, \tilde{P}\right).$$
 (26b)

where

$$A_0 := \begin{bmatrix} 0 & 1 & 0 \\ 0 & 0 & 1 \\ -c_0 & -c_1 & -c_2 \end{bmatrix}, \quad B_0 := \begin{bmatrix} 0 \\ 0 \\ \frac{A}{m} \end{bmatrix}. \tag{27}$$

Theorem 1. Let the control gains c_0 , c_1 , c_2 and parameter $\lambda > 0$ be selected to satisfy the conditions:

- The matrix A_0 is Hurwitz and the Lyapunov equation holds, i.e., $\Gamma A_0 + A_0^\top \Gamma = -\lambda I_{3\times 3}$, where $\Gamma = \Gamma^\top > 0$.
- ullet The parameter $arepsilon=rac{V_h}{eta}$ satisfy $0<arepsilon<arepsilon^*$ with

$$\varepsilon^* = \frac{\lambda m c_l}{\lambda |m c_2 - d| + 2|CA_0|\Gamma_3|_{\mathfrak{m}}},\tag{28}$$

where Γ_3 is the 3rd column of Γ .

Then the control law (15) and (20) will render the origin $(e, \tilde{P}) = (0, 0)$ of (26) globally exponentially stable.

Proof. To apply Lemma 1 to prove the system stability, all five conditions should be satisfied. Two Lyapunov function candidates are chosen as $V(e) = e^{\top} \Gamma e$ and $W(y) = \frac{1}{2} y^2$. Following Lemma 1, their time derivatives are given by

$$\frac{\partial V}{\partial e} f(e, \overline{\rho}(e)) = e^{\top} \left(\Gamma A_0 + A_0^{\top} \Gamma \right) e = -\lambda \left| e \right|^2, \tag{29}$$

$$\frac{\partial W}{\partial y}g(e, y + \overline{\rho}(e)) = -c_l|y|^2. \tag{30}$$

The equality in (29) holds by the Lyapunov equation. Hence, Condition 1 and 2 in Lemma 1 hold with $\alpha_1:=\lambda$, $\psi_1(x):=|e|$, $\alpha_2:=c_l$, and $\psi_2(y):=|y|$. For Condition 3, the bounding functions are simply chosen as $W_1=W_2=W$. Since $y+\overline{\rho}(e)=\tilde{P}$, Condition 4 holds with $\beta_1:=2\frac{A}{m}\Big|\Gamma_3\Big|_{\infty}$, such that

$$\frac{\partial V}{\partial e}[f(e, y + \overline{\rho}(e)) - f(e, \overline{\rho}(e))] = 2e^{\top} \Gamma B_0 y \le \beta_1 |e||y|. \tag{31}$$

Since $\frac{\partial W}{\partial a} = 0$, substituting (24) into Condition 5 yields

$$\begin{bmatrix}
\frac{\partial W}{\partial e} - \frac{\partial W}{\partial y} \frac{\partial \overline{\rho}}{\partial e}
\end{bmatrix} f(e, y + \overline{\rho}(e)) = -y \frac{\partial \overline{\rho}}{\partial e} (A_0 e + B_0 y) = y \frac{C}{A} \left(A_0 e + B_0 y \right) \le \frac{|CA_0|}{A} \left| e \right| \left| y \right| + \left| c_2 - \frac{d}{m} \right| \left| y \right|^2$$

$$= \beta_2 \psi_1(x) \psi_2(y) + \gamma \psi_2^2(y), \tag{32}$$

where $\beta_2 := \frac{|CA_0||}{A}$ and $\gamma := \left|c_2 - \frac{d}{m}\right|$. Hence, Condition 5 holds. All conditions hold globally for $\mathbb{D}_e = \mathbb{R}^3$ and $\mathbb{D}_{\tilde{p}} = \mathbb{R}$. After substituting the calculated $\alpha_1, \alpha_2, \beta_1, \beta_2$, and γ, ε^* is calculated as in Lemma 1 according to (28). It follows from [31] that $\mathscr{V}(e, \tilde{P}) = (1 - \delta)V(e) + \delta W(y)$, with a proper choice of $\delta > 0$, is a quadratic Lyapunov function for (26), proving that the origin $(e, \tilde{P}) = (0, 0)$ is globally exponentially stable.

Remark 1. In Eq. (28), ε^* is determined by the control gains C, λ , m, d, and c_l . When c_0 , c_1 , and c_2 are selected, ε^* increases with increasing c_l . The leakage, which occurs in any hydraulic systems, influences the equilibrium stability and cannot be avoided [38].

Remark 2. Considering $V_h = V_{h0} + Ah$, the system is stable when the length satisfies $h \leq \frac{\beta \mathcal{E}^* - V_{h0}}{A}$.

Remark 3. If we instead impose a setpoint regulation control problem, the desired trajectory h_r is set constant and its derivatives become zero, i.e., $\dot{h}_r = \ddot{h}_r = 0$. Considering also that $F_0 = mg$, then (19) becomes

$$\Psi(e_2) = -\left(\frac{d}{m} + A\Upsilon\right)e_2 + g. \tag{33}$$

Inserting this into (18), we get

$$\dot{e}_2 = \Upsilon u_0 - \left(\frac{d}{m} + A\Upsilon\right) e_2 + g + \frac{b}{m},\tag{34}$$

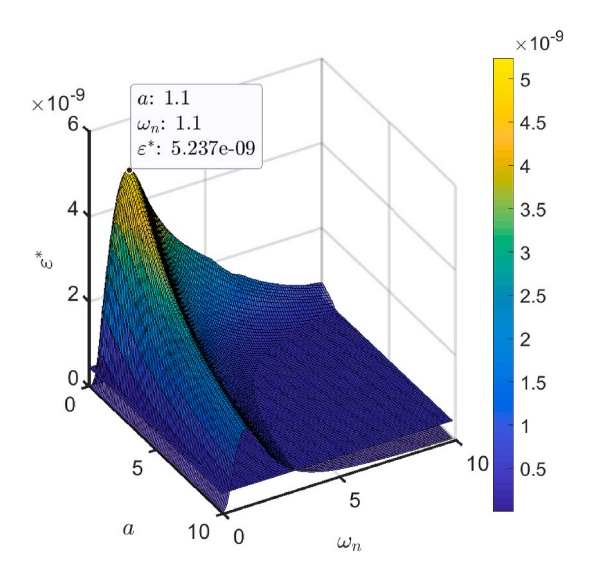


Fig. 5. The influence of the selected a and ω_n to ε^* in our case study. The maximum value of ε , in our case, is shown as the flat surface. For large values of both a and ω_n , where $\varepsilon > \varepsilon^*$, we notice that the control gains will invalidate the stability conditions of Theorem 1.

where Υ and $\frac{d}{m} + A\Upsilon$ are positive gains. It follows that a classical PID control

$$u_0 = -c_0 e_0 - c_1 e_1 - c_2 e_2, \tag{35}$$

by carefully tuning the PID gains, is sufficient to render the origin $(\tilde{e}, \tilde{P}) = (0, 0)$ exponentially stable, where the constant bias in $g + \frac{b}{m}$ will be compensated by the integrator.

Remark 4. The characteristic polynomial corresponding to A_0 in (27) is $s^3 + c_2 s^2 + c_1 s + c_0$. Let a desired closed-loop be given by $(s + a)(s^2 + 2\xi\omega_n s + \omega_n^2)$, where a > 0 is a desired real pole, $\xi > 0$ is a damping gain, and ω_n is a natural frequency. Matching these polynomials gives $c_0 = a\omega_n^2$, $c_1 = 2a\xi\omega_n + \omega_n^2$, and $c_2 = a + 2\xi\omega_n$. Choosing critical damping $\xi = 1.0$, as well as $\lambda = 1.0$, we investigate how the bound ε^* varies with different values of (a,ω_n) . This is shown in Fig. 5, for our case study, where it is seen that (28) reaches a maximum value of $\varepsilon^* \approx 5.24 \cdot 10^{-9}$ at $(a,\omega_n) \approx (1.1,1.1)$, whereas we have approximately $\varepsilon = \frac{V_h}{\beta} \in [0.25, 0.445] \cdot 10^{-9}$, shown as the flat surface in Fig. 5. This indicates that a sufficiently large range of feasible values for a and ω_n can be chosen while maintaining stability.

4. Simulation

4.1. Overview

The simulation is conducted in MATLAB/Simulink using MSS [39] and MarIn [40] toolboxes. The main parameters are summarized in Table 1. The lowering operation starts at 300 s. The proposed control system has been verified in the environmental conditions with significant wave height $H_s = \{1, 2, 3, 4, 5, 6\}$ m, wave period $T_p = \{4, 6, 8, 10, 12\}$ s, and wave direction $\beta_{wave} = \{0, 45, 90\}$ deg. In the first 300 s, the AHC compensates for the wave-induced relative displacement between the spar top and tower bottom with a constant distance. The lowering operation starts at 300 s. After reaching the mating height, the relative distance between the spar top and tower bottom is zero.

The coefficient ω_{r1} is tuned to make the lowering operation last for approximately 1 min. In our case study, $\omega_{r1}=0.1$ and $\omega_{r2}=80$. The control gains are selected as $(c_0,c_1,c_2)=(55,13,75)$, corresponding to $\alpha=3,\,\xi=1$, and $\omega_n=5$.

4.2. Simulation results

The controller effectively reduces the relative motion between the tower bottom and spar top. The time-domain simulation results are presented in Figs. 6 and 7.

From the simulation results, the trajectory planning module succeeds to generate a smooth trajectory in the entire process. From Fig. 6(a), the effects on the catamaran caused by the reacting force from the hydraulic system are small. The error between the real-time length and the reference signal remains within 0.05 m. The oscillation can be reduced by increasing the value $|\lambda|$ to achieve higher

Table 1Selected parameters in the simulations.

Parameter	Unit	Value
Catamaran length overall	m	144
Catamaran molded breadth	M	60
Catamaran draft	M	8.0
Displacement mass of the catamaran	Kg	1.85029e7
Vertical COG above baseline	M	28.6
OWT rated power	mW	10
Preassembly weight m_t	Kg	1.2e6
Hub height	M	115
Diameter of the spar at top	M	9.5
Diameter of the spar at waterline	M	14
Spar draft	M	96.3
Vertical position of COG	M	-51.8
Displacement mass of the spar	Kg	1.4906e7
Vertical position of fairlead	M	-15
Vertical position of mating point	M	20
Vertical center of gravity above keel	M	24.2
Vertical center of buoyancy above keel	M	47.3
Cylinder cross-section area A	m^2	0.39
Bulk modulus β	-	2e9
Fluid leakage coefficient c_l	-	1e-7
Mass of the hydraulic piston m_h	kg	1e3
Friction coefficient d	Ns/m	1e5
Volume of fluid in the pipeline V_0	m^3	0.5

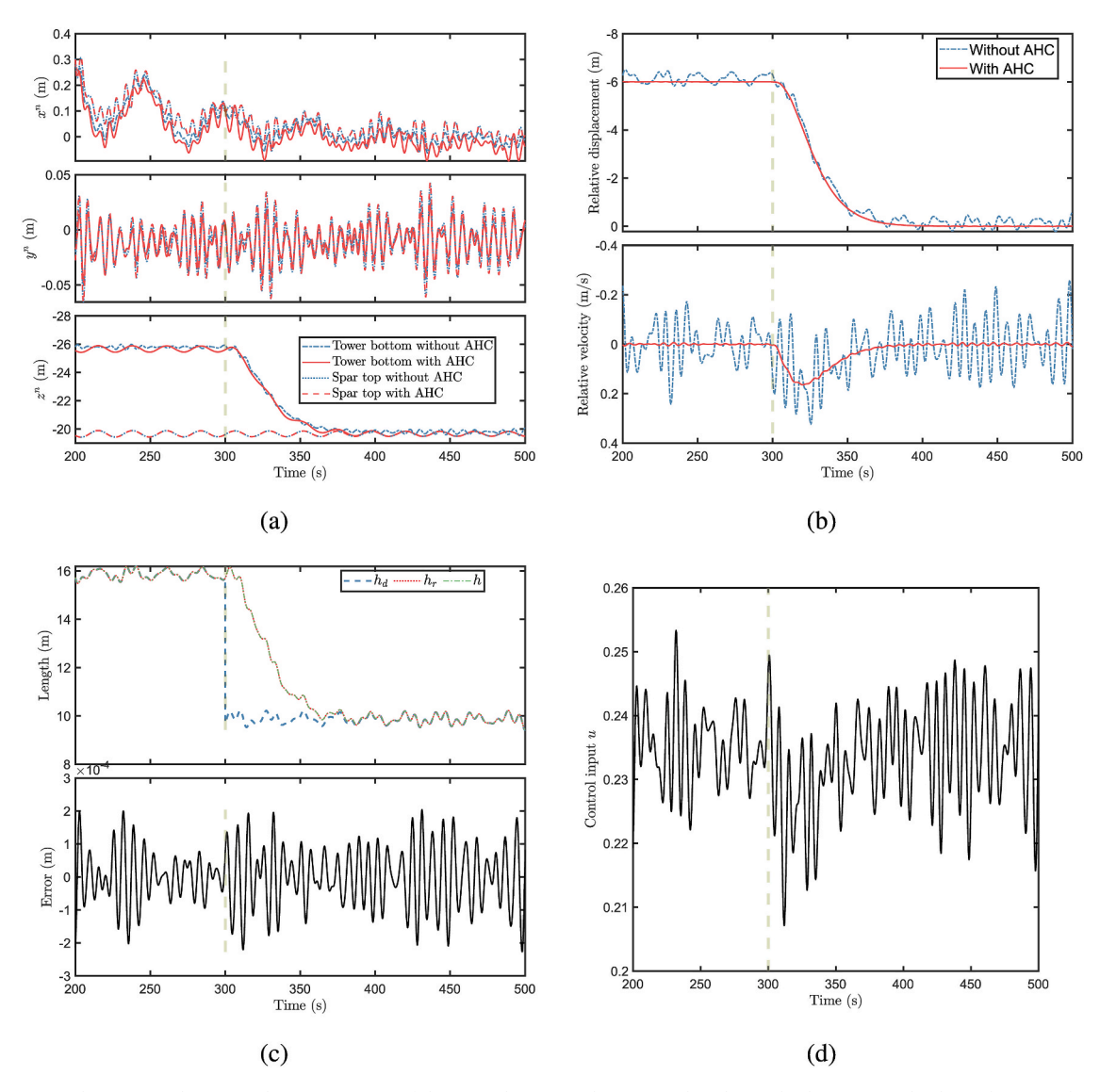


Fig. 6. Time-domain simulation results: (a) positions of the tower bottom and spar top; (b) relative displacement and velocity between the tower bottom and spar top; (c) path following performance of the hydraulic cylinder and the error between h and h_r ; (d) control input u. ($H_s = 1 \text{ m}$, $T_p = 6 \text{ s}$, and $\beta_{wave} = 0 \text{ deg.}$)

gains, which thus means more expensive equipment. The improvement to the relative velocity of the AHC is remarkable, as shown in Fig. 6(b). For the scenario with AHC, the relative velocity is normally less than 0.03 m/s, except the period 300–360 s. Since the AHC manages to cancel most relative velocity before 300 s and after 360s, it is easy to summary that the reason for the augment is the velocity used for the lowering operation. Using the proposed control system, the hydraulic cylinder follows the path well, as shown in Fig. 6(c). It is noticed from Fig. 6(d) that the control input is smooth and slowly varying.

The scenario in Fig. 7 is more critical than that in Fig. 6 due to the larger relative motion between the tower bottom and spar top. Even if the compensator lifts the preassembly onto the spar smoothly, there exist growing oscillations in the tracking error resulting from the increasing vessel motion; see Fig. 7(b). It is easy to show that the natural frequency of the vessel is higher than that of the spar foundation. Hence, the high-frequency motions result in inferior control accuracy.

4.3. Sensitivity study

The STDs and percentage reduction of a number of simulation results are presented in Fig. 8. In the figure, the bars denote the STD of the relative motion and the lines denote the motion percentage reduction. Each color block means a bar from zero to the top of the color block, i.e., the height of a color block denotes the additional values compared with that of its former wave height. The AHC succeeds to cancel the relative motion between the spar foundation and the assembly bottom. It decreases the relative displacement by

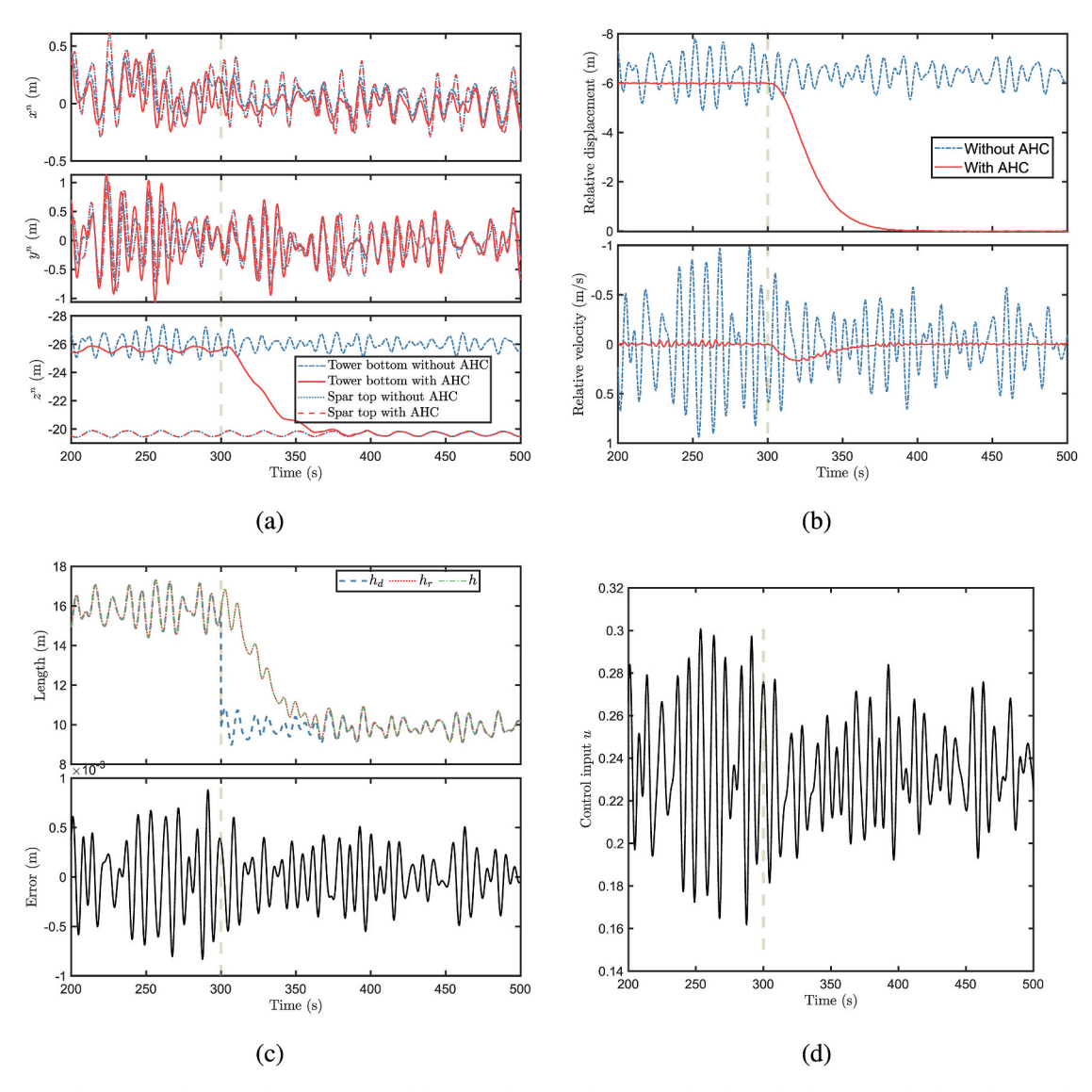


Fig. 7. Time-domain simulation results: (a) positions of the tower bottom and spar top; (b) relative displacement and velocity between the tower bottom and spar top; (c) path following performance of the hydraulic cylinder and the error between h and h_r ; (d) control input u. ($H_s = 2 \text{ m}$, $T_p = 10 \text{ s}$, and $\beta_{wave} = 45 \text{ deg.}$)

more than 95% and the relative velocity by more than 93% in most scenarios. When the relative motion is limited, for example $T_p = 4$ s, the percentage of relative motion compensation is smaller.

Comparing each group of bars indexed by "P" and "A" in Fig. 8, the STD of both the relative displacement and relative velocity increase with H_s in the scenarios without AHC. The wave period T_p has a larger influence on the relative motion. The relative motion between the spar top and tower bottom is the superposition of the wave-induced spar motion and vessel motion. Among the 12 DOF motions, the pitch motion of the catamaran and heave motion of both the catamaran and spar are important. The heave natural periods of the catamaran and the spar are approximately 6.5 s and 17.5 s, respectively. The roll and pitch natural periods of the catamaran are 9.1 s and 7.9 s, respectively 18. The amplitude of the wave-induced pitch and heave motions for the vessel and spar foundation increase when the wave period is close to their corresponding natural frequencies. More details of the system dynamics analysis could be found in 18.

However, the system capacity is limited by the physical design of the hydraulic system. As the maximum relative motion increases according to the significant wave height, the control system will start to struggle. It is not practical for the AHC to work under all sorts of environmental conditions when the amplitude of the relative motion surpasses the hydraulic cylinder length limitation. Therefore, planning and analysis should be conducted before practical operations.

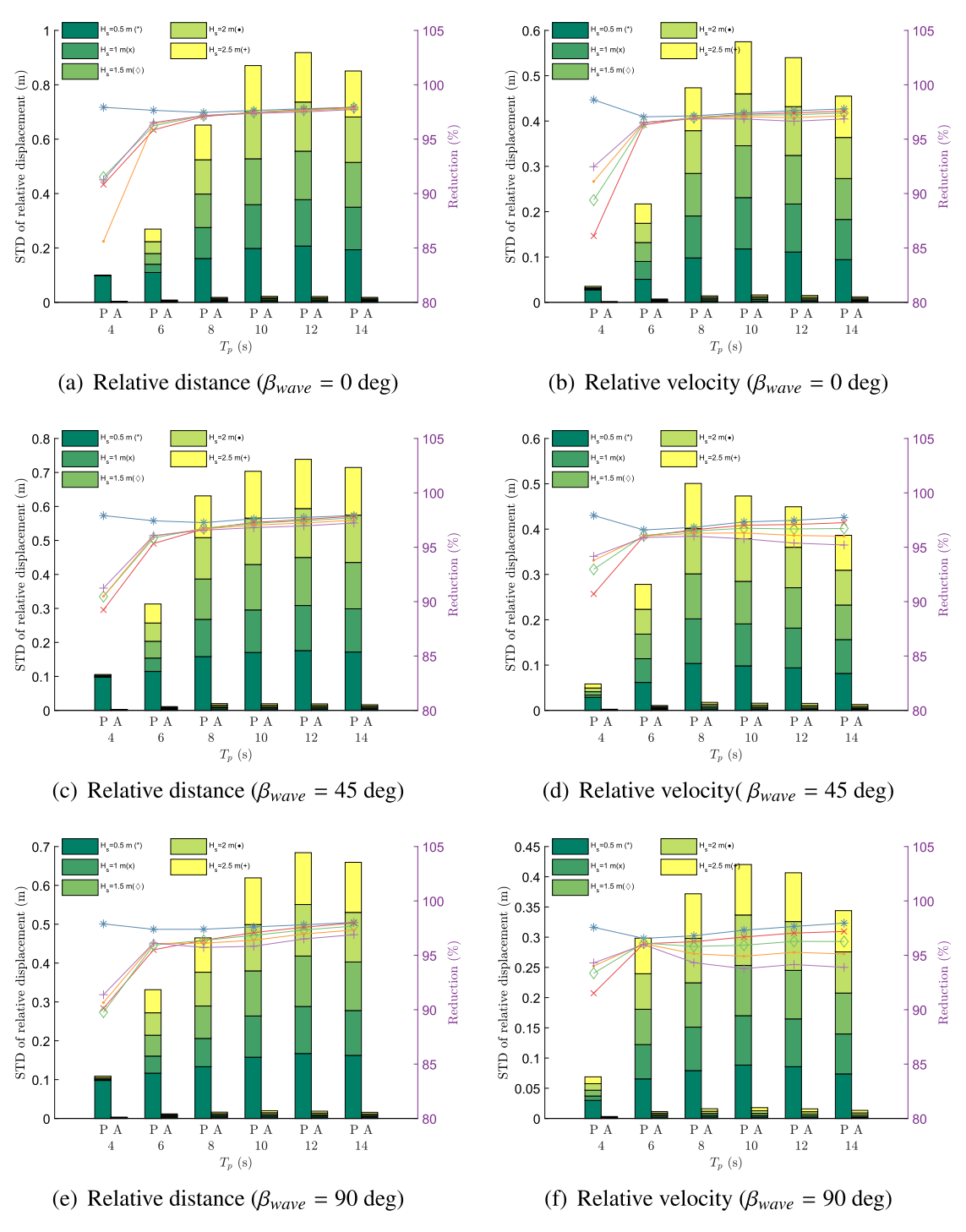


Fig. 8. The standard derivation (bars) and percentage reduction (lines with markers) of the relative displacement and relative velocity between the spar top and tower bottom, w.r.t., $H_s = \{1, 2, 3, 4, 5\}$ m, $T_P = \{4, 6, 8, 10, 12\}$ s, $\beta_{wave} = \{0, 45, 90\}$ deg (P - passive, A - active).

5. Conclusions

The automated wind turbine assembly installation approach is studied using a catamaran and an active hydraulic heave compensator. The fully coupled model is built in the MATLAB/Simulink environment. The trajectory planning module and control algorithm are developed. Two sections are included in the trajectory planning module for the hydraulic cylinder, i.e., to compensate for

the relative motion and to lower the preassembly. The control algorithm is designed according to singular perturbation theory. Simulation results show that the AHC greatly reduces the relative motion and relative velocity between the tower bottom and spar top in various sea states by controlling the hydraulic system. Verified by a sensitivity study, more than 95% and 93% relative displacement and relative velocity are reduced, respectively, in most scenarios. Hence, the AHC significantly broadens the operation window, improves the successful mating rate, and enhances the installation efficiency.

Declaration of competing interest

The authors declare that they have no known competing financial interests or personal relationships that could have appeared to influence the work reported in this paper.

Acknowledgment

This work was supported by the Research Council of Norway (RCN) through the Centre for Research-based Innovation on Marine Operations (CRI MOVE, RCN-project 237929).

References

- [1] Kaiser MJ, Snyder B. Offshore wind energy cost modeling: installation and decommissioning, vol. 85. Springer Science & Business Media; 2012.
- [2] Tang Y, Shi W, Ning D, You J, Michailides C. Effects of spilling and plunging type breaking waves acting on large monopile offshore wind turbines. Front, Mar. Sci 2020;7:427.
- [3] Nielsen JJ, Sørensen JD. On risk-based operation and maintenance of offshore wind turbine components. Reliab Eng Syst Saf 2011;96(1):218-29.
- [4] Sarker BR, Faiz TI. Minimizing maintenance cost for offshore wind turbines following multi-level opportunistic preventive strategy. Renew Energy 2016;85: 104–13.
- [5] Zhang L, Shi W, Karimirad M, Michailides C, Jiang Z. Second-order hydrodynamic effects on the response of three semisubmersible floating offshore wind turbines. Ocean Eng 2020;207:107371.
- [6] Vis IF, Ursavas E. Assessment approaches to logistics for offshore wind energy installation. Sustainable energy technologies and assessments 2016;14:80–91.
- [7] Sarker BR, Faiz TI. Minimizing transportation and installation costs for turbines in offshore wind farms. Renew Energy 2017;101:667-79.
- [8] Lacal-Arántegui R, Yusta JM, Domínguez-Navarro JA. Offshore wind installation: analysing the evidence behind improvements in installation time. Renew Sustain Energy Rev 2018;92:133–45.
- [9] Jiang Z, Gao Z, Ren Z, Li Y, Duan L. A parametric study on the final blade installation process for monopile wind turbines under rough environmental conditions. Eng Struct 2018;172:1042–56.
- [10] Gaunaa M, Bergami L, Guntur S, Zahle F. First-order aerodynamic and aeroelastic behavior of a single-blade installation setup. Journal of physics: conference series, vol. 524. IOP Publishing; 2014, 012073.
- [11] Verma AS, Vedvik NP, Gao Z. A comprehensive numerical investigation of the impact behaviour of an offshore wind turbine blade due to impact loads during installation. Ocean Eng 2019;172:127–45.
- [12] Gintautas T, Sørensen JD, Vatne SR. Towards a risk-based decision support for offshore wind turbine installation and operation & maintenance. Energy Procedia 2016;94:207–17.
- [13] Ren Z, Skjetne R, Gao Z. A crane overload protection controller for blade lifting operation based on model predictive control. Energies 2019;12(1):50.
- [14] Ren Z, Jiang Z, Skjetne R, Gao Z. An active tugger line force control method for single blade installations. Wind Energy 2018;21:1344–58.
- [15] Ren Z, Skjetne R, Jiang Z, Gao Z, Verma AS. Integrated GNSS/IMU hub motion estimator for offshore wind turbine blade installation. Mech Syst Signal Process 2019:123:222–43.
- [16] Tian X, Wang P, Li X, Wu X, Lu W, Wu C, Hu Z, Rong H, Sun H, Wang A, et al. Design and application of a monitoring system for the floatover installation. Ocean Eng 2018;150:194–208.
- [17] Hatledal LI, Zhang H, Halse KH, Hildre HP. Numerical study for a catamaran gripper-monopile mechanism of a novel offshore wind turbine assembly installation procedure. In: ASME 2017 36th international conference on ocean, offshore and arctic engineering-volume 9: offshore geotechnics; torgeir moan honoring symposium. American Society of Mechanical Engineers (ASME); 2017.
- [18] Jiang Z, Li L, Gao Z, Halse KH, Sandvik PC. Dynamic response analysis of a catamaran installation vessel during the positioning of a wind turbine assembly onto a spar foundation. Mar Struct 2018;61:1–24.
- [19] Xu J, Ren Z, Li Y, Skjetne R, Halse KH. Dynamic simulation and control of an active roll reduction system using free-flooding tanks with vacuum pumps. J Offshore Mech Arctic Eng 2018;140(6):061302.
- [20] Verma AS, Jiang Z, Ren Z, Gao Z, Vedvik NP. Response-based assessment of operational limits for mating blades on monopile-type offshore wind turbines. Energies 2019;12(10):1867.
- [21] Cheng X, Li G, Ellefsen AL, Chen S, Hildre HP, Zhang H. A novel densely connected convolutional neural network for sea state estimation using ship motion data. IEEE Transactions on Instrumentation and Measurement 2020;69(9):5984–93.
- [22] Niu H, Lu Y, Savvaris A, Tsourdos A. An energy-efficient path planning algorithm for unmanned surface vehicles. Ocean Eng 2018;161:308–21.
- [23] Zhu M, Sun W, Hahn A, Wen Y, Xiao C, Tao W. Adaptive modeling of maritime autonomous surface ships with uncertainty using a weighted LS-SVR robust to outliers. Ocean Eng 2020;200:107053.
- [24] Woodacre J. Bauer R. Irani R. A review of vertical motion heave compensation systems. Ocean Eng 2015;104:140–54.
- [25] Johansen TA, Fossen TI, Sagatun SI, Nielsen FG. Wave synchronizing crane control during water entry in offshore moonpool operations-experimental results. IEEE J Ocean Eng 2003;28(4):720–8.
- [26] Do KD, Pan J. Nonlinear control of an active heave compensation system. Ocean Eng 2008;35(5-6):558-71.
- [27] Knohl T, Unbehauen H. Adaptive position control of electrohydraulic servo systems using ANN. Mechatronics 2000;10(1–2):127–43.
- [28] Jiang Z, Ren Z, Gao Z, Sandvik PC, Halse KH, Skjetne R, et al. Mating control of a wind turbine tower-nacelle-rotor assembly for a catamaran installation vessel. In: The 28th international ocean and polar engineering conference. International Society of Offshore and Polar Engineers; 2018.
- [29] Ren Z, Zhao B, Nguyen DT. Finite-time backstepping of a nonlinear system in strict-feedback form: proved by Bernoulli inequality. IEEE Access 2020;8: 47768–75.
- [30] W. Deng, H. Liu, J. Xu, H. Zhao, Y. Song, An improved quantum-inspired differential evolution algorithm for deep belief network, IEEE Transactions on Instrumentation and Measurement .
- [31] Khalil HK. Noninear systems. 3 edn. New Jersey: Prentice-Hall; 2002.
- [32] Aamo OM, Fossen TI. Finite element modelling of mooring lines. Math Comput Simulat 2000;53(4-6):415-22.
- [33] Skjetne R, Ren Z. A survey on modeling and control of thruster-assisted position mooring systems. Mar Struct 2020;74:102830.
- [34] Wang L, Book WJ, Huggins JD. Application of singular perturbation theory to hydraulic pump controlled systems. IEEE ASME Trans Mechatron 2012;17(2): 251–9.

[35] Teel AR, Moreau L, Nesic D. A unified framework for input-to-state stability in systems with two time scales. IEEE Trans Automat Contr 2003;48(9):1526–44.
[36] Kokotovic P, Khali HK, O'reilly J. Singular perturbation methods in control: analysis and design, vol. 25. Siam; 1999.

- [37] Skjetne R, Teel AR, Kokotovic PV. Stabilization of sets parametrized by a single variable: application to ship maneuvering. In: Proc. 15th int. Symp. Mathematical theory of networks and systems; 2002.

 [38] Köster MA. On modeling, analysis and nonlinear control of hydraulic systems. Ph.D. thesis. Karlsruher Institut für Technologie (KIT); 2017.

 [39] Fossen TI, Perez T. Marine systems simulator (MSS). URL. 2014. https://github.com/cybergalactic/MSS.

- [40] Ren Z, Jiang Z, Skjetne R, Gao Z. Development and application of a simulator for offshore wind turbine blades installation. Ocean Eng 2018;166:380–95.